

# Three-Dimensional Printing of Hollow-Struts-Packed Bioceramic Scaffolds for Bone Regeneration

Yongxiang Luo,<sup>†,‡</sup> Dong Zhai,<sup>†</sup> Zhiguang Huan,<sup>†</sup> Haibo Zhu,<sup>§</sup> Lunguo Xia,<sup>||</sup> Jiang Chang,<sup>\*,†</sup> and Chengtie Wu<sup>\*,†</sup>

<sup>†</sup>State Key Laboratory of High Performance Ceramics and Superfine Microstructure, Shanghai Institute of Ceramics, Chinese Academy of Sciences, Shanghai 200050, China

<sup>‡</sup>Department of Biomedical Engineering, Health Science Center, Shenzhen University, Shenzhen 518060, China

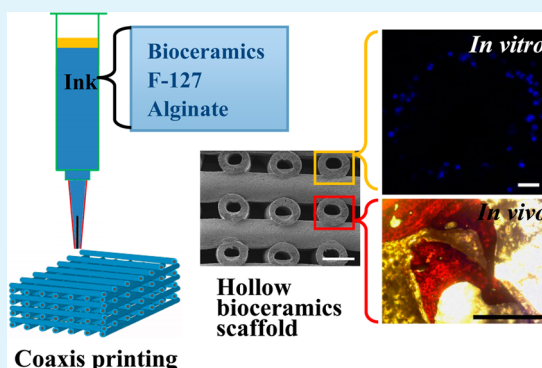
<sup>§</sup>Xuhui District Central Hospital, 966 Middle Huaihai Road, Shanghai 200000, China

<sup>||</sup>Center of Craniofacial Orthodontics, Department of Oral and Cranio-maxillofacial Science, School of Medicine, Ninth People's Hospital Affiliated to Shanghai Jiao Tong University, Shanghai 200011, China

## Supporting Information

**ABSTRACT:** Three-dimensional printing technologies have shown distinct advantages to create porous scaffolds with designed macropores for application in bone tissue engineering. However, until now, 3D-printed bioceramic scaffolds only possessing a single type of macropore have been reported. Generally, those scaffolds with a single type of macropore have relatively low porosity and pore surfaces, limited delivery of oxygen and nutrition to surviving cells, and new bone tissue formation in the center of the scaffolds. Therefore, in this work, we present a useful and facile method for preparing hollow-struts-packed (HSP) bioceramic scaffolds with designed macropores and multioriented hollow channels via a modified coaxial 3D printing strategy. The prepared HSP scaffolds combined high porosity and surface area with impressive mechanical strength. The unique hollow-struts structures of bioceramic scaffolds significantly improved cell attachment and proliferation and further promoted formation of new bone tissue in the center of the scaffolds, indicating that HSP ceramic scaffolds can be used for regeneration of large bone defects. In addition, the strategy can be used to prepare other HSP ceramic scaffolds, indicating a universal application for tissue engineering, mechanical engineering, catalysis, and environmental materials.

**KEYWORDS:** 3D printing, bioceramics, hollow-struts scaffolds, bone tissue engineering



## 1. INTRODUCTION

Treatment of critical-size bone defects caused by trauma, infection, and osteoporosis remains a significant clinical challenge.<sup>1</sup> An expected approach is to implant synthetic porous scaffolds into defects for guiding and stimulating formation of new bone tissues.<sup>2</sup> However, scaffold-based bone tissue engineering is still unable to effectively overcome some problems, such as poor host tissue integration and insufficient bone formation in the inner part of large bone defects due to the restrictions of homogeneous cell distribution, migration, and exchange of oxygen and nutrition to the inside of the scaffolds.<sup>3,4</sup> To address these issues, it is of great importance to design smart scaffolds with the ability to guide and stimulate formation of new bone tissue in large bone defects.<sup>5–8</sup> It is known that the nature of biomaterials plays a crucial role for satisfying this requirement,<sup>9,10</sup> in which the biological activity of scaffolds depends not only on material components but also on the macroporous architecture. Previous studies demonstrated that the geometrical features of porous scaffolds, including surface curvature, pore shape, and size, had a significant impact

on cellular response and in vivo bone regeneration.<sup>11–14</sup> Although modulating the geometrical features of scaffolds can partially improve their bone-forming ability, the strategy is far from optimal to effectively solve the long-term existing issue of insufficient bone formation in the inner part of large-size scaffolds. Several previous studies tried to solve these problems by creating hollow channels in scaffolds via a wire array template<sup>15,16</sup> and sacrificial modeling<sup>17,18</sup> strategies. In this process, porous silk scaffolds with mono-oriented hollow channels were prepared by freeze-drying in combination with a wire array template. The prepared hollow channels could facilitate cell infiltration. However, the methods were limited for preparing polymer-based scaffolds with mono-oriented hollow channels. In addition, the macropores in the scaffolds are uncontrollable by using the freeze-drying method.

**Received:** September 21, 2015

**Accepted:** October 19, 2015

**Published:** October 19, 2015

Herein, we reported a facile method to fabricate hollow-struts-packed (HSP) bioceramic scaffolds with designed macropores and multioriented hollow channel structures via coaxial 3D printing in order to enhance bone regeneration. Such novel scaffolds have significantly improved porosity and surface area for cell migration and new bone formation.

## 2. MATERIALS AND METHODS

**2.1. Three-Dimensional Printing of Hollow-Struts-Packed Bioceramic Scaffolds.** Bioceramic ( $\text{Ca}_7\text{Si}_2\text{P}_2\text{O}_{16}$ ) powders were synthesized by a sol–gel process using tetraethylorthosilicate ( $(\text{C}_2\text{H}_5\text{O})_4\text{Si}$ ), triethylphosphate ( $(\text{C}_2\text{H}_5\text{O})_3\text{PO}$ ), and calcium nitrate tetrahydrate ( $\text{Ca}(\text{NO}_3)_2 \cdot 4\text{H}_2\text{O}$ ) according to a previous study.<sup>19</sup> The received powders were grinded to a particle size less than  $38 \mu\text{m}$  by sieving through 400 mesh. To prepare the printable bioceramic ink (paste), 5 g of bioceramic powders was mixed with 0.3 g of alginate powder (Alfa Aesar) and 2.8 g of Pluronic F-127 (20 wt %) (Sigma-Aldrich) aqueous solution and then stirred until homogeneous pastes were achieved. HSP bioceramic scaffolds were fabricated by printing the prepared pastes through the design of a shell/core nozzle in the printing system (as shown in Figure 1a). The 3D printing system was

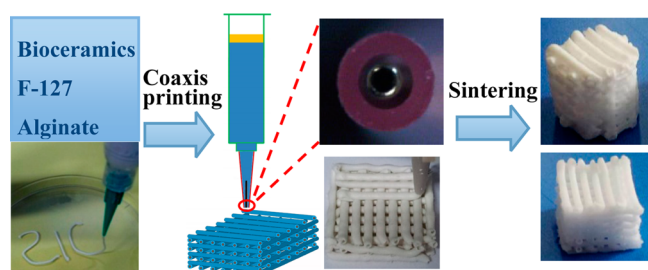


**Figure 1.** Procedure for the fabrication of HSP bioceramic scaffolds: by mixing bioceramic powders with F-127 solution (concentration: 20 wt %) and alginate to prepare printable inks, HSP bioceramic scaffolds were fabricated via coaxial printing of the prepared inks; the used coaxial printing nozzle is shown (20/27); after being sintered, the bioceramic scaffolds were mechanically stable, and the morphologies were designed.

developed by Fraunhofer IWS (Dresden, Germany) based on the Nano-Plotter device from GeSiM (Grosserkmannsdorf, Germany) and introduced on the market as a “bioscaffold printer”.<sup>20</sup> Solid-struts-packed (SSP) bioceramic scaffolds were printed based on a similar process only via signal nozzles and were used for controls. To control the porosity of the scaffolds, several sizes of shell/core nozzles were designed and prepared for this study, including those with a standards of (shell/core nozzle, G) 16/21, 16/22, 16/23, 18/25, and 20/27. After the scaffolds were printed, they were dried overnight at room temperature and then sintered at  $1400 \text{ }^\circ\text{C}$  for 3 h.

**2.2. Characterization of the Printed HSP Bioceramic Scaffolds.** The macropore and hollow channel morphology of the sintered scaffolds were observed by optical microscopy (S6D, Leica, Germany). The macropores and microstructure of the pore walls were characterized by scanning electron microscopy (SEM) (JSM-6700F, JEOL, Japan). The porosity was measured according to a liquid displacement method.<sup>21</sup> In brief, the scaffolds were first dried at  $100 \text{ }^\circ\text{C}$  overnight, weighed, and marked as  $M_1$ . Then, the scaffolds were immersed in water and placed under vacuum until no bubbles appeared. The weight of the scaffolds with water-filled pores was marked as  $M_2$ . Finally, the scaffolds were immersed in water, and the buoyant weight was marked as  $M_3$ . The porosity ( $P$ ) was calculated using the equation

$$P = (M_2 - M_1) / (M_2 - M_3) \times 100\%$$

**2.3. Mechanical Testing and in Vitro Degradation.** The compressive strength and modulus of the obtained scaffolds ( $10 \times 10$

$\times 10 \text{ mm}$ ) with different porosity (controlled by macropores and hollow channels) were tested using a computer-controlled universal testing machine (AG-I, Shimadzu, Japan) at a cross-head speed of  $0.5 \text{ mm min}^{-1}$ . Five samples were tested for each type of scaffold.

To compare the degradation of HSP and SSP scaffolds, two kinds of scaffolds (printed with a nozzle with a core/shell = 16/22) were soaked in Tris-HCl buffered solution (pH 7.40) in a shaking water bath at  $37 \text{ }^\circ\text{C}$  for 7, 14, 21, and 28 days. The solution was refreshed every 7 days. The ratio of solution volume to scaffold mass was  $50 \text{ mL g}^{-1}$ . Three samples were used for repeat experiments. At each time point, the weight loss was calculated. To investigate ionic release from the scaffolds, the solution was collected every 7 days. The concentrations of Ca, P, and Si ions were determined by inductively coupled plasma atomic emission spectrometry (ICP-AES) (Varian Co., USA).

**2.4. Cell Culture in Vitro.** Human bone marrow stem cells (BMSCs) (obtained from Cambrex, Walkersville, MD, USA) were seeded with an initial density of  $5 \times 10^4$  on each scaffold. The cell-seeded scaffolds were cultivated in an incubator at  $37 \text{ }^\circ\text{C}$  and 5%  $\text{CO}_2$ , and the cell culture medium was changed twice per week.

MTT assay was given after 1, 3, and 7 days of cultivation to analyze the proliferation of the cells on scaffolds. Briefly, 1 mL of the MTT solution ( $0.5 \text{ mg mL}^{-1}$  in cell culture medium) was added to each sample. After incubation for 4 h, the solution was removed and  $300 \mu\text{L}$  of DMSO (dimethylsulfoxide) was added to solubilize the formazan product. An aliquot of  $100 \mu\text{L}$  was transferred to a fresh 96-well plate; absorbance was measured at 590 nm in a microplate reader (Epoch microplate spectrophotometer, Bio Tek Instruments, USA). All the data are presented as optical density values minus the absorbance of blank wells. To prepare cell scaffold samples for SEM and confocal laser scanning microscopy analysis, after being washed with phosphate buffered saline and fixed with 2.5% glutaraldehyde, they were dried in hexamethyldisilazane for 30 min. Then, samples were coated with carbon and stained with rhodamine phalloidin-DAPI and observed by SEM (FEI Magellan 400) and confocal microscopy (Leica TCS SP8), respectively.

**2.5. In Vivo Evaluation.** All experiments were performed in compliance with the relevant laws and institutional guidelines. The HSP (printed by 16/22 nozzles) and SSP (printed by 16 nozzle) cylinder scaffolds with a size of  $\text{Ø}8 \times 10 \text{ mm}$  were implanted into femoral bone defects of adult New Zealand rabbits (nine rabbits with defects created both for right and left posterior limbs, Experimental Animal Center of Shanghai No. 1 Medical University, Shanghai, China) by surgery. General anesthesia was induced with an intravenous injection of 20% urethane ( $4 \text{ mL kg}^{-1}$ ). Critical size defects (8 mm diameter, 10 mm length) were transversally created in the interior of the distal femoral condyle of the posterior limbs by a standardized surgical procedure. The defects were prepared with an 8.0 mm drill. The depth of the defects was 10 mm as measured by a digital caliper. Then, one HSP and one SSP scaffold were implanted into the defect of the right and left posterior limbs in one rabbit, respectively. Afterward, four rabbits were sacrificed at 4 or 12 weeks randomly. The femoral–scaffold complex samples ( $n = 4$ ) were collected for micro-CT analysis immediately. The images were obtained via a Siemens Inveon micro-PET/CT scanner (Siemens Medical Solution, Germany). Mineralized tissue was distinguished from non-mineralized tissue via a global thresholding procedure with an approximate value of  $1.20 \text{ g cm}^{-3}$  (25% lower than  $1.6 \text{ g cm}^{-3}$ ). Only the region in the cylinder of the middle bone defect was measured. Bone volume in each defect was recorded as the measurement of new bone regeneration.

For histological analysis, all samples were fixed with 4% paraformaldehyde for 2 weeks and decalcified in 10% EDTA for 3 weeks. Then, samples were embedded in paraffin and cut using a microtome to yield  $300 \mu\text{m}$  thick sections. Afterward, the sections were stained with Van Gieson (VG) staining and then evaluated under light microscopy (Nikon, ECLIPSE E600).

**2.6. Statistical Analysis.** All data are expressed as means  $\pm$  standard deviations (SD) and were analyzed using one-way ANOVA, where  $p < 0.05$  was considered to be statistically significant.

### 3. RESULTS AND DISCUSSION

**3.1. Fabrication and Characterization of HSP Bioceramic Scaffolds.** To fabricate these HSP bioceramic scaffolds, two key factors should be carefully considered. One is to prepare the printable bioceramic paste (bioprinting ink), and the other is to design the coaxis (core-shell) printing nozzle. It is known that injectable polymer-based bioprinting ink is much easier to prepare than inorganic materials, due to the inherent rheological characteristic of polymers.<sup>22</sup> Compared to polymer-based scaffolds, bioceramic scaffolds have generally superior bioactivity for bone regeneration. However, it is quite difficult to prepare HSP bioceramic scaffolds via an extruding-based 3D printing method because the preparation of printable ink of bioceramics is one of the major challenges. Traditionally, the printable ink of ceramics (pastes) was mainly prepared by mixing ceramic powders with a certain concentration of polymer solution which could improve the viscosity and printability of ceramic ink. For example, SSP bioceramic scaffolds without hollow structures were fabricated via 3D printing based on the printable mixture ink of ceramic powders and poly(vinyl alcohol) or Pluronic F-127 solution.<sup>22–25</sup> However, the rheological characteristics and mechanical strength (stability during printing) of the prepared bioceramic inks by conventional methods cannot be used for printing HSP bioceramic scaffolds that require quite critical printing conditions, mainly including highly rheological and mechanically stable ceramic paste. Therefore, a modified printable bioceramic ink was developed in this study by introducing 3–5 wt % alginate in this system to improve their rheological and mechanical properties. Alginate is a biocompatible material that can form a stable hydrogel when in contact with dications such as  $\text{Ca}^{2+}$ .<sup>20,26</sup> After addition of a certain amount of alginate (3–5 wt %) in the inks of bioceramic powders and polymer solutions (e.g., 20 wt % Pluronic F-127), a stable bioceramic ink composed of powders, alginate, and F-127 was formed. The mass ratio of ceramic powders, alginate, and F-127 plays a critical role for preparing the printable bioceramic inks. As shown in Figure 1, after the bioceramic ink-based scaffolds were printed by the 3D coaxis printing method, they were then sintered at 1400 °C for 3 h to remove the alginate and F-127 phases, and the bioceramic particles were densified to form HSP bioceramic scaffolds (Figure 1). The HSP scaffolds still maintained the designed pore structures, including macropores (outside of struts) and open hollow channels (inside of struts), despite 25% longitudinal shrinkage and around 57.8% volume shrinkage occurring for the whole scaffolds after high-temperature sintering at 1400 °C. X-ray diffraction (XRD) analysis indicated that alginate and Pluronic F-127, as the solution of bioceramic ink, have no obvious effect on the final crystal phase composition of HSP bioceramic scaffolds, which still maintained pure ceramic phase of  $\text{Ca}_7\text{P}_2\text{Si}_2\text{O}_{16}$  (JCPD 11-0676) (Figure 2). According to JCPD 11-0676, the XRD pattern indicated the clear crystal phase of  $\text{Ca}_7\text{Si}_2\text{P}_2\text{O}_{16}$ . After being sintered under high temperature, the bioceramic has no change of crystal composition. Besides the preparation of printable bioceramic ink, the design of a coaxis nozzle is the other key factor for printing HSP bioceramic scaffolds. In this study, the coaxis nozzle was constructed by inserting a right angle stainless steel nozzle with a smaller diameter (core nozzle) into a conic plastic nozzle with a larger diameter (shell nozzle) (as shown in Figure 1). The size and geometries of the hollow struts can be controlled by the coaxis nozzle. By using

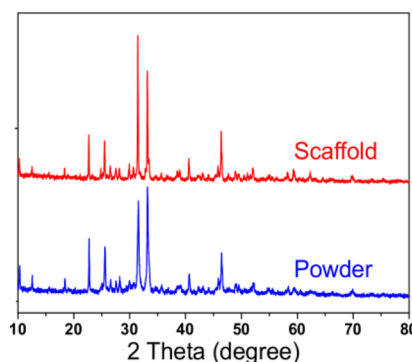


**Figure 2.** XRD analysis of bioceramic powders and the prepared HSP scaffolds after sintering.

different sizes of coaxis nozzle, the size of hollow struts, including the outer size, inner size (hollow channel), and the thickness of struts, could be well-controlled (Figure 3). In addition, by designing the shape of the inner nozzle, the geometries of hollow struts could be well-prepared with circle, square, and even other complicated geometries (Figure 3). By using these methods, other HSP bioceramic scaffolds, such as  $\beta$ -tricalcium phosphate, can be effectively prepared. In addition, other HSP ceramic scaffolds can also be prepared by using this method, indicating that the strategy for the modified ceramic ink and the design of a coaxis nozzle stands is an effective method to construct 3D-printed HSP ceramic scaffolds not only for biomedical application but also for mechanical engineering and catalysis application.

The printed HSP bioceramic scaffolds had designed macropores (outside of struts, controlled by CAD design) and multioriented hollow channel structures (inside of struts, controlled by core/shell nozzle). The macropores and hollow channels were completely opened (Figure 3). Compared to the printed SSP scaffolds, the total porosity and specific surface area of HSP scaffolds were significantly enhanced. The HSP scaffolds printed by the coaxis nozzle with a standard of 20G/27G (shell/core nozzle standard) had high porosity up to 86% and high specific surface area up to 6500  $\text{mm}^2/\text{g}$ , while the printed SSP scaffolds with similar macropores by the nozzle with a standard of 20G had only 57% porosity and 2800  $\text{mm}^2/\text{g}$  specific surface area. The porosity of HSP scaffolds was nearly 30% higher than that of SSP scaffolds, and the specific surface area of HSP scaffolds was 2.3 times that of SSP scaffolds. In addition, the porosity of HSP scaffolds can be well-controlled from 65 to 85% by adjusting the core/shell size of the printing nozzles (Figure 4). Therefore, the mechanical properties of HSP scaffolds can be effectively controlled by controlling their porosity via the core/shell size ratio, in which the compressive strength ( $\sim 5$  MPa) and modulus ( $\sim 160$  MPa) of HSP scaffolds with a core/shell size of 16/23 are comparable to those of the SSP scaffolds (Figure 5). In addition, the compressive strength and modulus of HSP scaffolds are 4–6 times those of bioceramic scaffolds (with similar porosity) prepared by the foam template method,<sup>27,28</sup> which is a widely used conventional method to prepare bioceramic scaffolds for bone tissue engineering. Furthermore, the compressive strength of HSP scaffolds is comparable with that of 3D-printed hollow-channel brushite and monetite scaffolds with lower porosity (only 38 and 44%, respectively) (compressive strength:  $7.47 \pm 0.7$  and  $1.47 \pm 0.2$  MPa, respectively).<sup>29</sup> The results suggest that HSP bioceramic scaffolds have significantly superior mechanical

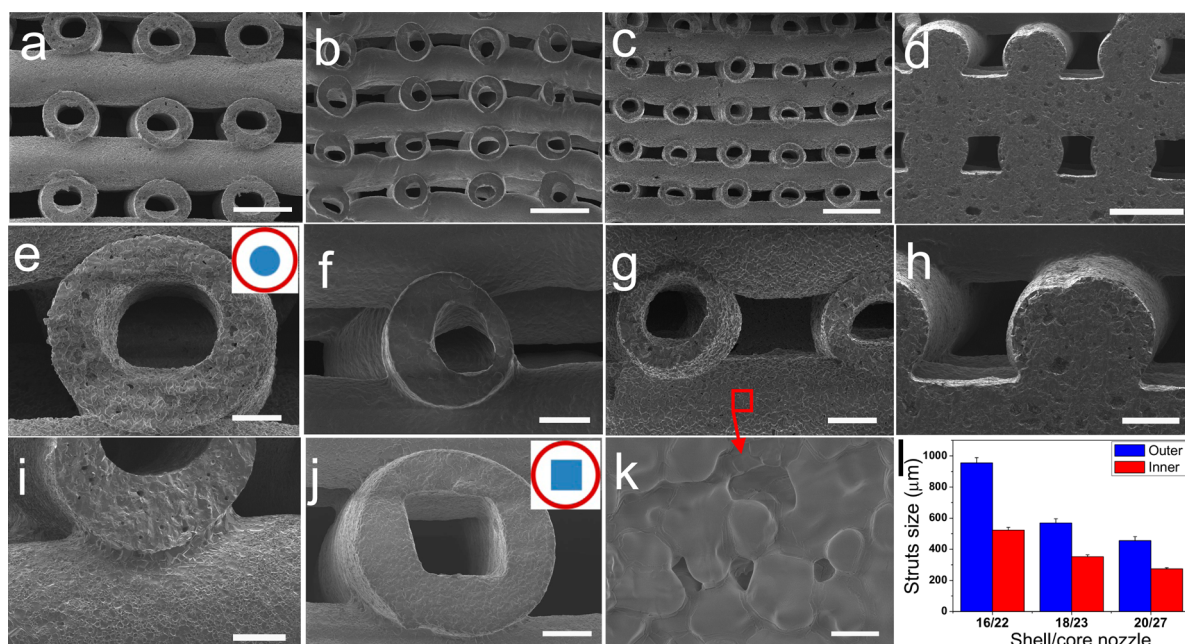


**Figure 3.** SEM images of printed HSP bioceramic scaffolds via core/shell nozzle of 16/22 (a,e), 18/23 (b,f), and 20/27 (c,g) and printed SSP bioceramic scaffolds (d,h) as the control. Strong binding between hollow struts in different layers after sintering (i). Hollow strut with square (j) morphology and high-magnification SEM for the dense strut surface (k). The relationship of strut sizes for the printed HSP scaffolds with different core/shell nozzles of printers (l). The scale bar was 1 mm (a–d), 200  $\mu\text{m}$  (e–j), and 20  $\mu\text{m}$  (k).

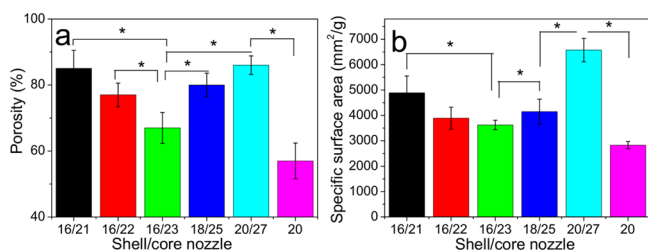


**Figure 4.** Porosity (a) and specific surface area (b) of the printed HSP (16/21, 16/22, 16/23, 18/25, and 20/27) scaffolds can be easily controlled by varying the core/shell ratio of printer nozzles, which further modulates the mechanical strength of the prepared scaffolds.

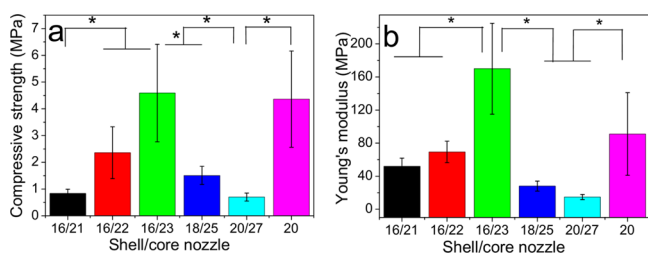


**Figure 5.** Compressive strength (a) and Young's modulus (b) of printed HSP scaffolds with different porosity via different core/shell nozzles. Printed SSP scaffold (20) as control was evaluated ( $*p < 0.05$ ).

strength as compared to hollow polymer scaffolds prepared by the previously used wire array template method. It is known that the compressive strength of cancellous bone is about 2–12 MPa. The compressive strength of HSP scaffolds is comparable with that of cancellous bone, suggesting that the strength of HSP scaffolds is sufficient for non-load-bearing application of bone regeneration.

### 3.2. Attachment and Proliferation of Cells on Printed Scaffolds.

Our previous studies have confirmed that the prepared bioceramic ( $\text{Ca}_7\text{Si}_2\text{P}_2\text{O}_{16}$ ) powder, disk, and 3D scaffolds had no obvious cytotoxicity and presented good cytocompatibility with bone marrow stromal cells.<sup>19,21,24,30,31</sup> However, compared to those scaffolds without hollow channel structures, one of the significant advantages for the prepared HSP bioceramic scaffolds is that their high porosity and surface area lead to distinctively improved cell attachment and migration of BMSCs in the inner part of the scaffolds. Tissue engineering scaffolds with high porosity and surface area were preferred for cell adherence, migration, and exchange of gas and nutrition as well as tissue regeneration.<sup>14,32</sup> In this study, BMSCs were seeded through the vertical sectional of HSP scaffolds with different strut sizes. SSP scaffolds were used for the controls. It was found that BMSCs adhered not only on the outer surface of hollow struts but also on the inner surface of hollow struts (Figure 6). Compared to SSP scaffolds with same size of macropores, HSP scaffolds had significantly improved cell attachment at day 3 and proliferation at day 7 (Figure 6). It is reasonable to speculate that the improved porosity and surface area of HSP scaffolds mainly contributed to the distinctively high cell proliferation level. In addition, the hollow channels in the HSP scaffolds may be a benefit for enhancing oxygen and nutrient distribution in the inner part of the scaffolds and further improve cell infiltration and proliferation in the scaffolds.<sup>15,16,33</sup>

**3.3. Bone Formation in Vivo.** One of most interesting results is that the printed HSP bioceramic scaffolds have superior bone-forming ability in vivo. According to the obtained results in vitro, the HSP scaffolds of 16/22 had porosity and compressive strength and modulus comparatively higher than that of other types of HSP scaffolds. Therefore, in this study, the printed HSP (nozzle standard: 16/22) bioceramic scaffolds with a size of  $\text{Ø}8 \times 10 \text{ mm}$  (Figure 7a) were chosen to implant in the femur defect of rabbits (Figure

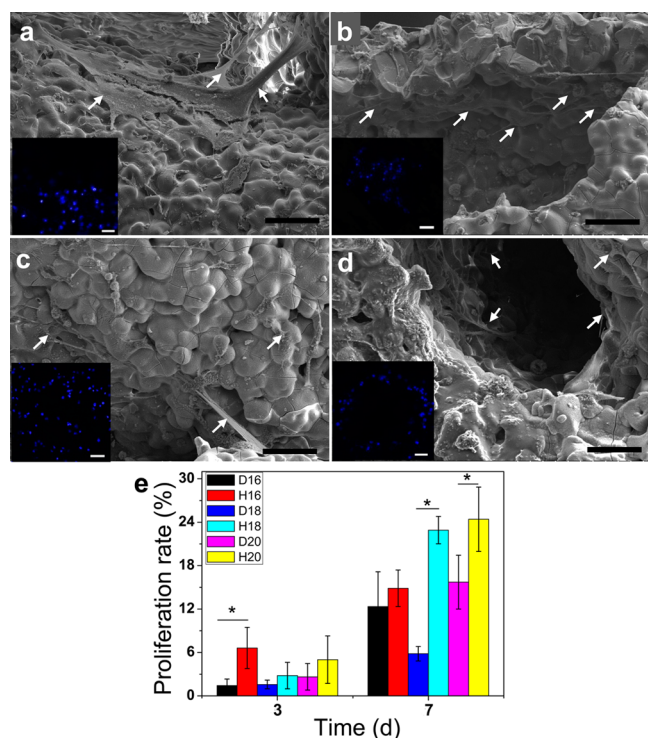


**Figure 6.** SEM images of BMSCs seeded in printed HSP bioceramic scaffolds on day 1 (a,b) and day 7 (c,d). Cells attached on the outside of the strut surface of scaffolds (a,c) and inside of hollow struts (b,d). Inset images show the confocal laser scanning microscope images of cells in scaffolds (blue = DAPI staining). The proliferation (e) of cells in printed scaffolds. (D16, D18, and D20 mean solid-strut-packed scaffolds with printing nozzle sizes of 16G, 18G, and 20G, respectively; H16, H18, and H20 mean hollow-strut-packed scaffolds with printing nozzle sizes of 16/22G, 18/25G, and 20/27G, respectively). White arrows indicate the cells. Scale bar = 50  $\mu\text{m}$  ( $*p < 0.05$ ).

7b) to investigate the new bone-formation ability in vivo. SSP (nozzle standard: 16) scaffolds with the same macropores were used for the controls. Four weeks after implantation, micro-CT analysis showed that the HSP scaffolds integrated well with the host bone tissue, and new bone tissue started to grow into the porous scaffold, while there was limited new bone tissue growing into the porous SSP scaffold (Figure 7). VG staining results indicated that the new bone tissues not only formed in the macropores but also grew into the hollow channels of HSP scaffolds (Figure 8). Furthermore, it was found that there were

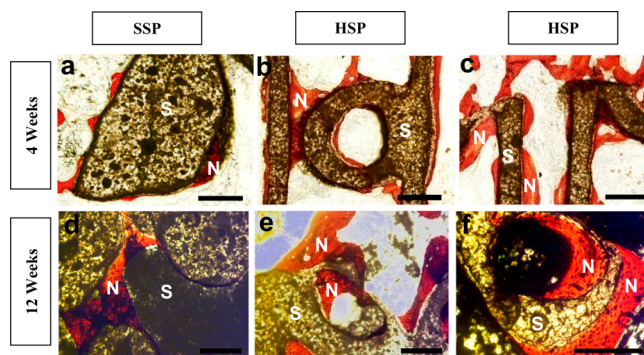


**Figure 8.** Histological images for SSP (a,d) and HSP (b,c,e,f) scaffolds were taken at week 4 (a–c) and week 12 (d–f) after operation (S indicates scaffolds; N indicates new bone tissue). Scale bar = 300  $\mu\text{m}$ .

great amounts of newly formed bone tissue in the center of the HSP bioceramic scaffolds, while nearly no obvious new bone tissue was observed in the center of SSP scaffolds at week 4. After 12 weeks of implantation, the new bone tissue in the hollow channels of the HSP scaffold grew much thicker than that at week 4, and in the meanwhile, the hollow strut wall became much thinner due to the degradation of scaffolds (Figure 8). Although an amount of ions were released and pore wall was thinned during degradation, the HSP scaffolds still maintained their regular hollow channel structures to support

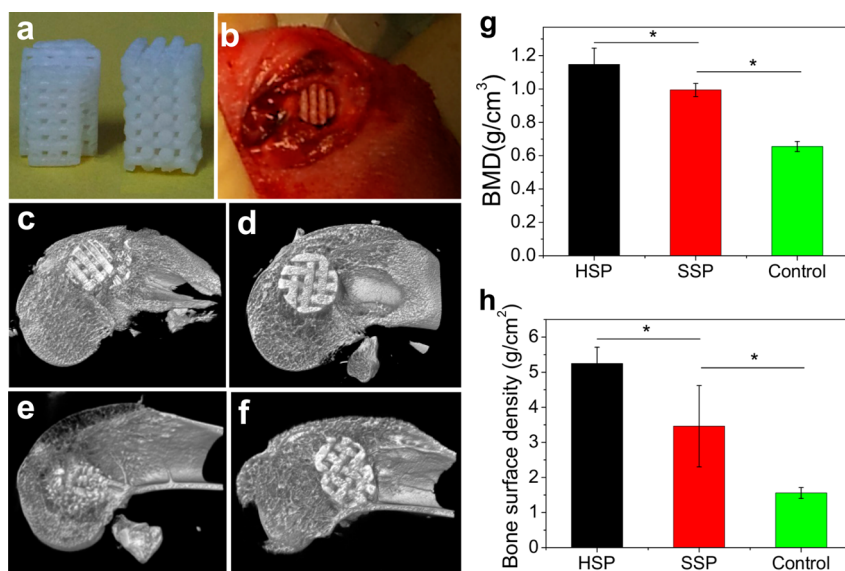


**Figure 7.** Image of printed scaffolds (left, HSP scaffolds; right, SSP scaffolds ( $\varnothing 8 \times 10$  mm)) for in vivo experiment (a). HSP scaffold (hollow) after implanted in the femur of rabbits (b). Micro-CT analysis of in vivo bone-formation ability of HSP scaffolds (c,e) and SSP scaffolds (d,f) for 4 (c,d) and 12 (e,f) weeks. The BMD (g) and bone surface density (h) of samples (control: no scaffolds) after implanted in vivo for 12 weeks. It is obvious that HSP bioceramic scaffolds significantly stimulate new bone formation as compared to SSP bioceramic scaffolds ( $*p < 0.05$ ).

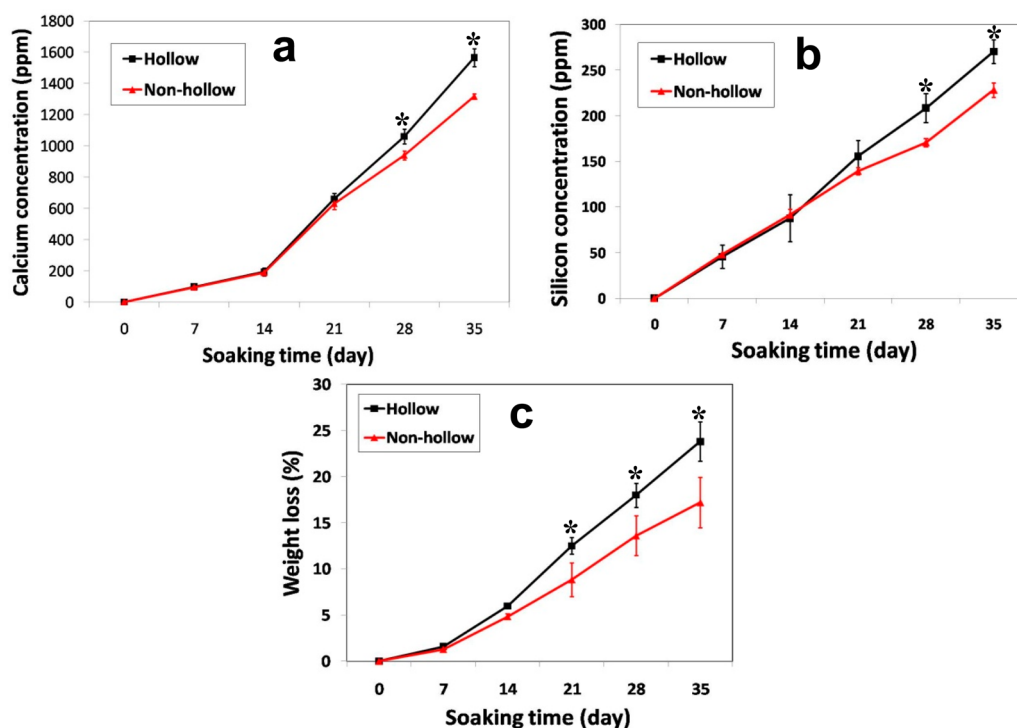


**Figure 9.** Calcium (a) and silicon (b) ions release from HSP and SSP scaffolds and weight loss (c) of printed HSP (hollow) and SSP (nonhollow) bioceramic scaffolds in Tris-HCl buffer at 37 °C over 5 weeks.

newly bone tissue ingrowth. Micro-CT analysis further showed that the bone mineral density (BMD) and bone surface density of HSP scaffolds were significantly higher than those of SSP scaffolds and control samples (without scaffolds). All the obtained data showed that the new bone tissue not only formed in the macropores of HSP scaffolds but also grew along their hollow channels of struts, indicating that the hollow channels in the scaffold struts play an important role in guiding new bone formation in vivo.

Compared to SSP bioceramic scaffolds, which are the general types of scaffolds obtained via 3D printing, novel HSP bioceramic scaffolds prepared in this work have several distinct properties due to their hollow channel structures. First, HSP scaffolds had higher porosity and specific surface area, which provides more space and surface for cell infiltration and new bone formation. Second, HSP bioceramic scaffolds had faster degradation rate due to their larger surface area and higher porosity. ICP analysis indicated that more ions (Ca and Si) were released from HSP scaffolds than from SSP scaffolds (Figure 9). Previous studies showed that Si ions had the ability to promote osteogenesis as compared to  $\beta$ -tricalcium phosphate ( $\beta$ -TCP).<sup>34–36</sup> In this study, the improved bone regeneration of HSP bioceramic scaffolds may be directly related to the quick release of Si ions from the scaffolds. In addition, the improved degradation of HSP scaffolds may offer much more room for growth of new bone tissue.<sup>7</sup> Furthermore, the multioriented hollow struts with tube structures provided a bridge role for transferring oxygen and nutrition and cell migration. Compared to mono-oriented hollow channels with embedded scaffolds created via a template, multioriented HSP scaffolds printed in this work could recruit cells from all around the host tissues and deliver oxygen and nutrition from different directions of the scaffolds, which may benefit the improvement of bone formation.

#### 4. CONCLUSION

In summary, in this work, we presented a useful and facile method for preparing HSP bioceramic scaffolds with designed macropores and multioriented hollow channels via a modified coaxial 3D printing strategy. The prepared HSP scaffolds combined high porosity and surface area with impressive mechanical strength. The unique hollow-strut structures of bioceramic scaffolds significantly improved cell attachment and proliferation and further promoted formation of new bone in the center of the scaffolds, indicating that HSP ceramic scaffolds can be used for reservation of large bone defects. In addition, the strategy can be used for prepare other HSP ceramic scaffolds (e.g.,  $ZrO_2$ ), indicating a potential application for tissue engineering, mechanical engineering, catalysis, and environmental materials.

#### ■ ASSOCIATED CONTENT

##### 📄 Supporting Information

The Supporting Information is available free of charge on the ACS Publications website at DOI: 10.1021/acsami.5b08911.

Figure S1 (PDF)

#### ■ AUTHOR INFORMATION

##### Corresponding Authors

\*E-mail: [jchang@mail.sic.ac.cn](mailto:jchang@mail.sic.ac.cn). Tel: +86-21-52412804. Fax: +86-21-52413903.

\*E-mail: [chengtiewu@mail.sic.ac.cn](mailto:chengtiewu@mail.sic.ac.cn). Tel: +86-21-52412249. Fax: +86-21-52413903.

##### Notes

The authors declare no competing financial interest.

## ACKNOWLEDGMENTS

This study was funded by the Shanghai Municipal Natural Science Foundation (14ZR1445500) and the Natural Science Foundation of China (Grants 31400807, 31370963). The National High Technology Research and Development Program of China (863 Program, SS2015AA020302) and Shanghai Outstanding Leaders' project (15XD1503900) provided partial support.

## REFERENCES

- (1) Calori, G. M.; Mazza, E.; Colombo, M.; Ripamonti, C. The use of bone-graft substitutes in large bone defects: Any specific needs? *Injury* **2011**, *42*, 56–63.
- (2) Liu, Y.; Lim, J.; Teoh, S. H. Review: Development of clinically relevant scaffolds for vascularised bone tissue engineering. *Biotechnol. Adv.* **2013**, *31*, 688–705.
- (3) Laschke, M. W.; Harder, Y.; Amon, M.; Martin, I.; Farhadi, J.; Ring, A.; Torio-padron, N.; Schramm, R.; Rucker, M.; Junker, D.; Haufel, J. M.; Carvalho, C.; Heberer, M.; Germann, G.; Vollmar, B.; Menger, M. D. Angiogenesis in Tissue Engineering: Breathing Life into Constructed Tissue Substitutes. *Tissue Eng.* **2006**, *12*, 2093–2104.
- (4) Stevens, M. M. Biomaterials for bone tissue engineering. *Mater. Today* **2008**, *11*, 18–25.
- (5) Bose, S.; Roy, M.; Bandyopadhyay, A. Recent advances in bone tissue engineering scaffolds. *Trends Biotechnol.* **2012**, *30*, 546–554.
- (6) Luo, Y.; Lode, A.; Akkineni, A. R.; Gelinsky, M. Concentrated gelatin/alginate composites for fabrication of pre-designed scaffolds with favorable cell response by 3D plotting. *RSC Adv.* **2015**, *5*, 43480–43488.
- (7) Neffe, A. T.; Pierce, B. F.; Tronci, G.; Ma, N.; Pittermann, E.; Gebauer, T.; Frank, O.; Schossig, M.; Xu, X.; Willie, B. M.; Forner, M.; Ellinghaus, A.; Lienau, J.; Duda, G. N.; Lendlein, A. One Step Creation of Multifunctional 3D Architected Hydrogels Inducing Bone Regeneration. *Adv. Mater.* **2015**, *27*, 1738–1744.
- (8) Wang, M. O.; Vorwald, C. E.; Dreher, M. L.; Mott, E. J.; Cheng, M. H.; Cinar, A.; Mehdizadeh, H.; Somo, S.; Dean, D.; Brey, E. M.; Fisher, J. P. Evaluating 3D-Printed Biomaterials as Scaffolds for Vascularized Bone Tissue Engineering. *Adv. Mater.* **2015**, *27*, 138–144.
- (9) Williams, D. F. On the nature of biomaterials. *Biomaterials* **2009**, *30*, S897–S909.
- (10) Pina, S.; Oliveira, J. M.; Reis, R. L. Natural-Based Nano-composites for Bone Tissue Engineering and Regenerative Medicine: A Review. *Adv. Mater.* **2015**, *27*, 1143–1169.
- (11) Bidan, C. M.; Kommareddy, K. P.; Rumpler, M.; Kollmannsberger, P.; Fratzl, P.; Dunlop, J. W. Geometry as a Factor for Tissue Growth: Towards Shape Optimization of Tissue Engineering Scaffolds. *Adv. Healthcare Mater.* **2013**, *2*, 186–194.
- (12) Zadpoor, A. A. Bone tissue regeneration: the role of scaffold geometry. *Biomater. Sci.* **2015**, *3*, 231–245.
- (13) Van Bael, S.; Chai, Y. C.; Truscetto, S.; Moesen, M.; Kerckhofs, G.; Van Oosterwyck, H.; Kruth, J. P.; Schrooten, J. The effect of pore geometry on the in vitro biological behavior of human periosteum-derived cells seeded on selective laser-melted Ti6Al4V bone scaffolds. *Acta Biomater.* **2012**, *8*, 2824–2834.
- (14) Karageorgiou, V.; Kaplan, D. Porosity of 3D biomaterial scaffolds and osteogenesis. *Biomaterials* **2005**, *26*, 5474–5491.
- (15) Rnjak-Kovacina, J.; Wray, L. S.; Golinsky, J. M.; Kaplan, D. L. Arrayed Hollow Channels in Silk-Based Scaffolds Provide Functional Outcomes for Engineering Critically Sized Tissue Constructs. *Adv. Funct. Mater.* **2014**, *24*, 2188–2196.
- (16) Zhang, W.; Wray, L. S.; Rnjak-Kovacina, J.; Xu, L.; Zou, D.; Wang, S.; Zhang, M.; Dong, J.; Li, G.; Kaplan, D. L.; Jiang, X. Vascularization of hollow channel-modified porous silk scaffolds with endothelial cells for tissue regeneration. *Biomaterials* **2015**, *56*, 68–77.
- (17) Yu, T. T.; Shoichet, M. S. Guided cell adhesion and outgrowth in peptide-modified channels for neural tissue engineering. *Biomaterials* **2005**, *26*, 1507–1514.
- (18) Nazhat, S. N.; Neel, E. A.; Kidane, A.; Ahmed, I.; Hope, C.; Kershaw, M.; Lee, P. D.; Stride, E.; Saffari, N.; Knowles, J. C.; Brown, R. A. Controlled Microchannelling in Dense Collagen Scaffolds by Soluble Phosphate Glass Fibers. *Biomacromolecules* **2007**, *8*, 543–551.
- (19) Zhou, Y.; Wu, C.; Xiao, Y. The stimulation of proliferation and differentiation of periodontal ligament cells by the ionic products from Ca<sub>2</sub>Si<sub>2</sub>P<sub>2</sub>O<sub>16</sub> bioceramics. *Acta Biomater.* **2012**, *8*, 2307–2316.
- (20) Luo, Y.; Lode, A.; Wu, C.; Chang, J.; Gelinsky, M. Alginate/nano-hydroxyapatite scaffolds with designed core/shell structures fabricated by 3D plotting and in situ mineralization for bone tissue engineering. *ACS Appl. Mater. Interfaces* **2015**, *7*, 6541–6549.
- (21) Xu, M.; Zhai, D.; Chang, J.; Wu, C. In vitro assessment of three-dimensionally plotted nagelschmidtitite bioceramic scaffolds with varied macropore morphologies. *Acta Biomater.* **2014**, *10*, 463–476.
- (22) Luo, Y.; Lode, A.; Gelinsky, M. Direct plotting of three-dimensional hollow fiber scaffolds based on concentrated alginate pastes for tissue engineering. *Adv. Healthcare Mater.* **2013**, *2*, 777–783.
- (23) Wu, C.; Luo, Y.; Cuniberti, G.; Xiao, Y.; Gelinsky, M. 3D-Printing of hierarchical and tough mesoporous bioactive glass scaffolds with controllable pore architecture, excellent mechanical strength and mineralization ability. *Acta Biomater.* **2011**, *7*, 2644–2650.
- (24) Xu, M.; Li, H.; Zhai, D.; Chang, J.; Chen, S.; Wu, C. Hierarchically porous nagelschmidtitite bioceramic–silk scaffolds for bone tissue engineering. *J. Mater. Chem. B* **2015**, *3*, 3799–3809.
- (25) Franco, J.; Hunger, P.; Launey, M. E.; Tomsia, A. P.; Saiz, E. Direct write assembly of calcium phosphate scaffolds using a water-based hydrogel. *Acta Biomater.* **2010**, *6*, 218–228.
- (26) Augst, A. D.; Kong, H. J.; Mooney, D. J. Alginate hydrogels as biomaterials. *Macromol. Biosci.* **2006**, *6*, 623–633.
- (27) Wu, C.; Chang, J.; Zhai, W.; Ni, S.; Wang, J. Porous akermanite scaffolds for bone tissue engineering: Preparation, characterization, and in vitro studies. *J. Biomed. Mater. Res., Part B* **2006**, *78B*, 47–55.
- (28) Wu, C.; Ramaswamy, Y.; Zreiqat, H. Porous diopside (CaMgSi<sub>2</sub>O<sub>6</sub>) scaffolds: A promising bioactive material for bone tissue engineering. *Acta Biomater.* **2010**, *6*, 2237–2245.
- (29) Habibovic, P.; Gbureck, U.; Doillon, C. J.; Bassett, D. C.; van Blitterswijk, C. A.; Barralet, J. E. Osteoconduction and osteoinduction of low-temperature 3D printed bioceramic implants. *Biomaterials* **2008**, *29*, 944–953.
- (30) Wu, C.; Fan, W.; Chang, J.; Zhang, M.; Xiao, Y. Preparation, characterization and in vitro bioactivity of nagelschmidtitite bioceramics. *J. Am. Ceram. Soc.* **2013**, *96*, 928–934.
- (31) Wu, C.; Han, P.; Xu, M.; Zhang, Y.; Zhou, Y.; Xue, G.; Chang, J.; Xiao, Y. Nagelschmidtitite bioceramics with osteostimulation properties: material chemistry activating osteogenic genes and WNT signaling pathway of human bone marrow stromal cells. *J. Mater. Chem. B* **2013**, *1*, 876–885.
- (32) Loh, Q. L.; Choong, C. Three-dimensional scaffolds for tissue engineering applications: Role of porosity and pore size. *Tissue Eng., Part B* **2013**, *19*, 485–502.
- (33) Moroni, L.; Schotel, R.; Sohler, J.; de Wijn, J. R.; van Blitterswijk, C. A. Polymer hollow fiber three-dimensional matrices with controllable cavity and shell thickness. *Biomaterials* **2006**, *27*, 5918–5926.
- (34) Sun, H.; Wu, C.; Dai, K.; Chang, J.; Tang, T. Proliferation and osteoblastic differentiation of human bone marrow-derived stromal cells on akermanite-bioactive ceramics. *Biomaterials* **2006**, *27*, 5651–5657.
- (35) Wu, C.; Fan, W.; Zhou, Y.; Luo, Y.; Gelinsky, M.; Chang, J.; Xiao, Y. 3D-printing of highly uniform CaSiO<sub>3</sub> ceramic scaffolds: preparation, characterization and in vivo osteogenesis. *J. Mater. Chem.* **2012**, *22*, 12288–12295.
- (36) Han, P.; Wu, C.; Xiao, Y. The effect of silicate ions on proliferation, osteogenic differentiation and cell signalling pathways (WNT and SHH) of bone marrow stromal cells. *Biomater. Sci.* **2013**, *1*, 379–392.